



**HAL**  
open science

## Enhanced EBSD calibration accuracy based on gradients of diffraction patterns

Qiwei Shi, Hongru Zhong, Dominique Loisonard, Lei Wang, Zhe Chen, Haowei Wang, Stéphane Roux

### ► To cite this version:

Qiwei Shi, Hongru Zhong, Dominique Loisonard, Lei Wang, Zhe Chen, et al.. Enhanced EBSD calibration accuracy based on gradients of diffraction patterns. *Materials Characterization*, 2023, 202, pp.113022. 10.1016/j.matchar.2023.113022 . hal-04490189

**HAL Id: hal-04490189**

**<https://hal.science/hal-04490189>**

Submitted on 5 Mar 2024

**HAL** is a multi-disciplinary open access archive for the deposit and dissemination of scientific research documents, whether they are published or not. The documents may come from teaching and research institutions in France or abroad, or from public or private research centers.

L'archive ouverte pluridisciplinaire **HAL**, est destinée au dépôt et à la diffusion de documents scientifiques de niveau recherche, publiés ou non, émanant des établissements d'enseignement et de recherche français ou étrangers, des laboratoires publics ou privés.

# Enhanced EBSD calibration accuracy based on gradients of diffraction patterns

Qiwei Shi<sup>1,2</sup>, Hongru Zhong<sup>2</sup>, Dominique Loisonard<sup>3</sup>, Lei Wang<sup>2</sup>,

Zhe Chen<sup>2</sup>, Haowei Wang<sup>2</sup>, Stéphane Roux<sup>4</sup>

1: SJTU-Paris Elite Institute of Technology,

Shanghai Jiao Tong University, Shanghai, 200240, China

2: School of Materials Science and Engineering,

Shanghai Jiao Tong University, Shanghai, 200240, China

3: EDF R&D, Site des Renardières, avenue des Renardières,  
Ecuelles, F-77818 Moret-sur-Loing, France

4: Université Paris-Saclay, CentraleSupélec, ENS Paris-Saclay, CNRS,  
LMPS - Laboratoire de Mécanique Paris-Saclay, F-91190, Gif-sur-Yvette, France

Aug 30, 2023

## Abstract

High-resolution electron backscatter diffraction (HR-EBSD) attracts increasing attention in materials researches, and correlating simulated and experimental diffraction patterns is a major HR-EBSD branch. However, the correlation accuracy is limited by several secondary effects generally not accounted for in pattern simulations, such as the non-uniform electron energy, Kikuchi band (K-band) asymmetry or gray level reversal. Although some of these phenomena can be simulated by Monte Carlo method and dynamical simulation, the computation is highly demanding and their effects on EBSD calibration are not systematically analyzed. Recently, it has been shown that the precise locations of K-band edges were better identified using the gradient of the diffraction patterns, in particular with the presence of K-band asymmetry. In the present study, it is proposed to use a similar strategy, in Integrated Digital Image Correlation to circumvent the systematic errors, and lack of accuracy due to these asymmetry artefacts. Gray level profiles of the K-bands are analyzed to assess the correctness of image registration. High-definition experimental EBSD datasets show that crystal orientation uncertainty improves by  $0.01^\circ$  when using gradients. Another evidence of the enhanced calibration accuracy is the improved continuity of the calibrated projection center position at grain boundaries by about 50%. In view of these results, it is suggested to systematically resort to gradients of diffraction patterns in all high-resolution EBSD analyses when correlating experimental and simulated patterns.

**Keyword:** EBSD calibration, High-angular-resolution EBSD, Integrated digital image correlation, Kikuchi band asymmetry, Digital image processing.

Table 1: List of notations used in the paper

$(X, Y, Z)$ collectively as $\mathbf{X}$	Coordinates in the sample reference
$(x, y, z)$ collectively as $\mathbf{x}$	Coordinates in the EBSD detector's reference
$(x^*, y^*, z^*)$ collectively as $\mathbf{x}^*$	Coordinates of the projection center in the detector's reference
$\Delta(x^*, y^*, z^*)$ collectively as $\Delta\mathbf{x}^*$	Difference of projection center coordinates by different calibration methods
$\delta(x^*, y^*, z^*)$ collectively as $\delta\mathbf{x}^*$	Deviation of projection center coordinates to its linear fitted fields
$(u, v)$ collectively as $\mathbf{u}$	Coordinates in the stereographically projected master pattern
$(\varphi_1, \phi, \varphi_2)$	Euler angle triplet
$\theta$	Angle to the diffracting crystal plane, downwards the EBSP chosen as positive
$\theta_B$	Angle to the diffracting crystal plane fulfilling the Bragg's equation
$\tilde{\theta}$	Defined as $\theta/\theta_B$
$b$	Integers enumerating the diffracting plane of Kikuchi bands

## 1 Introduction

Electron BackScatter Diffraction (EBSD), a module in scanning electron microscopes, is a common technique to obtain crystallographic orientation in crystalline samples. It provides orientation maps from the analysis of the Kikuchi diffraction pattern (Electron BackScatter Pattern, denoted as EBSP hereinafter) by various algorithms [1, 2, 3]. The Hough transformation algorithm is the most used for its efficiency and availability [1]. Standard EBSD usually has a spatial resolution of tens of nanometers and an angular resolution of about  $0.5^\circ$ . This angular uncertainty level enables standard EBSD to evaluate the orientation maps, but elastic strains and small angle grain boundaries are beyond its reach.

High-(angular) Resolution EBSD (HR-EBSD) has been proposed to obtain *relative* crystallographic orientations with a much higher accuracy [4, 5]. It consists in matching high-definition EBSP pairs by Digital Image Correlation (DIC). HR-EBSD estimates the elastic strains with acceptable uncertainties at excellent spatial resolution [6]. The *local* DIC algorithm based on cross-correlation is employed in HR-EBSD in the first place [4], followed by several (*integrated*) *global* DIC frameworks [7, 8, 9, 10]. The latter method proves fast and precise, as it treats the whole pattern without subset overlapping or remapping [9]. Yet the results of HR-EBSD are limited by the accuracy of the projection center (PC) coordinates [11, 9], regardless of the correlation algorithms.

Hardware and software based methods are two ways to address EBSD calibration. The former ones need specific devices during acquisition, such as a standard sample of known orientation [12], a mobile EBSP detector [13, 14, 15, 16], or a mask of special shape in front of the detector [17]. Software-based EBSD calibrations have drawn increasing interests in recent years thanks to their precision, usability and versatility. One conventional way is

to identify multiple K-bands and analyze the geometry of their diffracting planes [18, 19, 20]. Another software-based calibration is the full pattern match (FPM), whose basic idea is to tune the projection parameters (and in particular the three coordinates of the PC) in order to maximize the similarity between experimental and *simulated* EBSPs, especially the *dynamically* simulated ones [21]. Many optimization algorithms have been adopted in FPM [22, 23, 24, 26, 27, 25, 28, 29], and they all contribute significantly to the EBSD calibration progress in recent years. The PC calibration uncertainty, tested on simulated EBSPs, reaches values as low as  $10^{-5}$  times the pattern width for simulated EBSPs [27, 28], though the calibration accuracy level on *experimental* patterns remains to be assessed.

The calibration accuracy can be estimated by comparing hardware and software calibration methods, or by judging the correctness of the obtained whole PC fields. For example, different groups studying software EBSD calibration have reported apparent grainwise discontinuities, up to 1-2 pixels, in PC fields [25, 28]. This irregularity indicates the flaw of matching experimental EBSP with the projection of the pre-calculated master pattern [30]. In fact, several secondary effects in experimental EBSPs should be considered in FPM. For example, the signal-to-noise ratio and brightness of Kikuchi band are closely linked to the sample tilt angle, and that smaller than  $60^\circ$  could even lead to reversed gray level distributions [31]. The correction of radial optical distortion of the EBSD camera helps reducing PC discontinuities [32]. Recent studies have also reported the inhomogeneous distribution of diffracted electron energy [33], explicitly, the energy of diffracted electrons on the top side of EBSP is several keV lower than that of the bottom side. Another well-known phenomenon is the Excess-Deficiency (ED), (upper edges of K-bands are brighter than lower ones), as a result of the anisotropy of the distribution of diffracted electrons [34]. These secondary effects need to be accounted for, otherwise *systematic* errors will result in PC and crystal orientation for software EBSD calibration methods. The nonphysical discontinuity of PC at grain boundaries is a firm indicator of calibration error. Note that varying strain levels and surface roughness due to etching artifacts and slip activities are examples of ‘physical’ PC discontinuities.

The aforementioned secondary effects of experimental EBSPs can be addressed in dynamical simulations, and offers a better similitude with experimental EBSPs [34, 31] and improved calibration results [35]. However, the simulated EBSP of different PC or crystal orientations require lengthy and dedicated calculations, rather than a quick projection from an once-computing master pattern. As a result, simple and fast methods to correct these EBSP imperfections are in need for FPM-based EBSD analyses.

The gradient operation is a common signal processing method that emphasizes local differences of the signal (at short wavelength) and dampens the effect of long wavelength modulations. Computing gradients has been adopted in recent years in the EBSD community for various goals. Alkorta *et al.* [36], calculate the gradients of EBSP in both directions in full pattern matching to facilitate positioning the cross-correlation peaks, which are sharper than those of the original EBSP patterns cross-correlation. The Sobel operator (*i.e.*, a variant of the gradient operator over a slightly extended neighborhood as compared to finite differences) is also used in EBSD analysis to calculate image gradients and locate the K-bands precisely [1, 19]. Saowadee *et al.* [37] have proposed to define the Kikuchi band edge (corresponding to the Bragg’s angle) as the extreme points of the 1st derivative. This criterion works well even with the excess-deficit phenomenon, thus providing an objective method to locate the band edge and get the band width. This method has since been adopted by Nolze *et al.* [38] to extract the lattice constants from

EBSP.

The present work proposes to apply a gradient filter to both experimental and simulated EBSPs in order to mitigate the effect of ED, then rely on the IDIC framework for calibrating EBSD, including refinement of both crystal orientation and PC position. Section 2 details the proposed gradient-based analysis. Section 3 calibrates the high-resolution EBSPs of a macroscopically unstrained dual phase sample, and compares the calibration results with a hardware-based EBSD calibration method. Section 4 shows the algorithm performance on high-resolution EBSPs of a polycrystalline Al alloy captured with varying tilt angles. Section 5 shows the algorithm performance on a 10% strained polycrystalline Al alloy. The gradient filter enhances the accuracy of indexed Euler angles and the PC coordinates for all 3 cases.

## 2 Reduction of K-band asymmetry by gradient operation

### 2.1 Algorithm of IDIC-G EBSD

The projection geometry of EBSP is recalled in figure 1 together with the reference system used in the paper. The notations are also listed in Table 1.

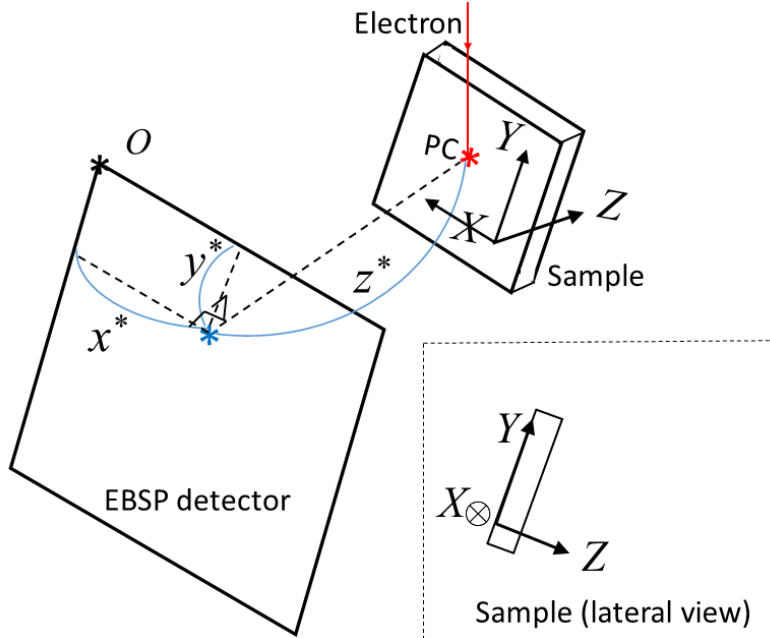


Figure 1: Coordinate systems  $(x, y, z)$  associated to EBSP detector and  $(X, Y, Z)$  associated to sample

The EBSP screen is chosen as the reference defining the  $(x, y)$  plane, or  $z = 0$ . The origin of the  $(x, y)$  plane is noted as  $O$ . The unit vector  $\mathbf{w}$  linking the projection center to each pixel  $\mathbf{x} = (x, y, z = 0)$  of the screen [28] is

$$\mathbf{w} = \frac{(\mathbf{x} - \mathbf{x}^*)}{|\mathbf{x} - \mathbf{x}^*|} \quad (1)$$

In order to rotate the vector  $\mathbf{w}$  to that of the spherical master pattern,  $\mathbf{w}'$ , one should multiply it by a rotation

operator  $\mathbf{Q}$  corresponding to the crystal orientation as stated in Ref [28]

$$\mathbf{w}' = \mathbf{Q}\mathbf{w} \quad (2)$$

whose expression involves the Euler angles:

$$\mathbf{Q} = \begin{bmatrix} \cos \varphi_1 \cos \varphi_2 - \sin \varphi_1 \sin \varphi_2 \cos \phi & \sin \varphi_1 \cos \varphi_2 + \cos \varphi_1 \sin \varphi_2 \cos \phi & \sin \varphi_2 \sin \phi \\ -\cos \varphi_1 \sin \varphi_2 - \sin \varphi_1 \cos \varphi_2 \cos \phi & -\sin \varphi_1 \sin \varphi_2 + \cos \varphi_1 \cos \varphi_2 \cos \phi & \cos \varphi_2 \sin \phi \\ \sin \varphi_1 \sin \phi & -\cos \varphi_1 \sin \phi & \cos \phi \end{bmatrix} \quad (3)$$

The stereographical projection of  $\mathbf{w}'$  onto the master pattern plane,  $\mathbf{u}$ , is written as in Ref [28]

$$\mathbf{u} = \frac{\mathbf{w}' - \mathbf{n}}{(1 - \mathbf{w}' \cdot \mathbf{n})} + \mathbf{n} \quad (4)$$

where  $\mathbf{n} = (0, 0, 1)^\top$  stands for a unit vector pointing at the north pole. The projected position  $\mathbf{u}(\mathbf{x})$  can be expressed explicitly as a function of  $\mathbf{x}$  and of the projection parameters  $(\varphi_1, \phi, \varphi_2, x^*, y^*, z^*)$  collectively noted as  $\mathbf{P}$ . The effect of elastic strain on the EBSP is neglected here.

Then the IDIC EBSD procedure described in Ref. [28] is adapted to register the gradient images with limited changes. To distinguish from the normal IDIC EBSD, the method described in the current paper is named as IDIC-G EBSD (Integrated Digital Image Correlation for the Gradients of EBSP). From this point and on, EBSD is omitted after IDIC or IDIC-G for brevity.

From the EBSP  $f(x, y)$ , the two components of the gradient  $f_{,x}$  and  $f_{,y}$  are computed

$$f_{,x}(x, y) = \frac{\partial f(x, y)}{\partial x}, f_{,y}(x, y) = \frac{\partial f(x, y)}{\partial y} \quad (5)$$

In the IDIC EBSD algorithm, experimental EBSP  $f(\mathbf{x})$  is chosen as the reference, while in IDIC-G EBSD calibration the two components of the gradient (Equation 5) are used as references simultaneously. The dynamically simulated EBSP pattern is  $g(\mathbf{x})$ , which is projected from the simulated master pattern  $G(\mathbf{u})$  by the relation  $g(\mathbf{x}) = G(\mathbf{u}(\mathbf{x}, \mathbf{P}))$ . The IDIC-G algorithm involves matching at best  $f_{,x}(\mathbf{x})$  and  $g_{,x}(\mathbf{x})$ ,  $f_{,y}(\mathbf{x})$  and  $g_{,y}(\mathbf{x})$  at the same time, through the minimization of a quadratic norm of the residuals  $r_{x,y}$  summed over the entire ROI. The cost function to minimize is written

$$\Theta = \sum_{ROI} \omega(\mathbf{x})^2 \left\{ [f_{,x}(\mathbf{x}) - g_{,x}(\mathbf{x})]^2 + [f_{,y}(\mathbf{x}) - g_{,y}(\mathbf{x})]^2 \right\} \quad (6)$$

where  $g(\mathbf{x})$  is the current estimate of simulated EBSP during iterative algorithms,  $\omega(\mathbf{x})$  is the weight associated to the noise level of each pixel (an example is given in Section 4). Note that this cost function with gradient operation is equivalent to that adopted by Alkorta *et al.* [36], which stores the gradients in both directions as a complex number for cross-correlation uses. The cost function (6) is iteratively minimized with a Gauss-Newton algorithm. Starting from an approximate solution, the transformation  $\mathbf{u}(\mathbf{x})$  is progressively corrected with linear combinations of sensitivity fields constituting the kinematic basis [39].

The gradients  $g_{,x}$  and  $g_{,y}$  can be computed efficiently from  $G_{,u}$  and  $G_{,v}$ , the gradients of circular master pattern in  $\mathbf{u}$  space, using the chain rule

$$g_{,x}(\mathbf{x}) = G_{,u}(\mathbf{u}) \frac{\partial u}{\partial x} + G_{,v}(\mathbf{u}) \frac{\partial v}{\partial x}, \quad g_{,y}(\mathbf{x}) = G_{,u}(\mathbf{u}) \frac{\partial u}{\partial y} + G_{,v}(\mathbf{u}) \frac{\partial v}{\partial y} \quad (7)$$

The zoomed master pattern  $G(\mathbf{u})$  is shown in Figure 2a, and its gradient  $G_{,\bullet}$  are shown in Figures 2b-2c respectively. Note that  $\frac{\partial \mathbf{u}}{\partial \mathbf{x}}$  are smooth functions of  $\mathbf{P}$ , as a result their derivatives with respect to  $\mathbf{P}$  are ignored in the Gauss-Newton formulas.

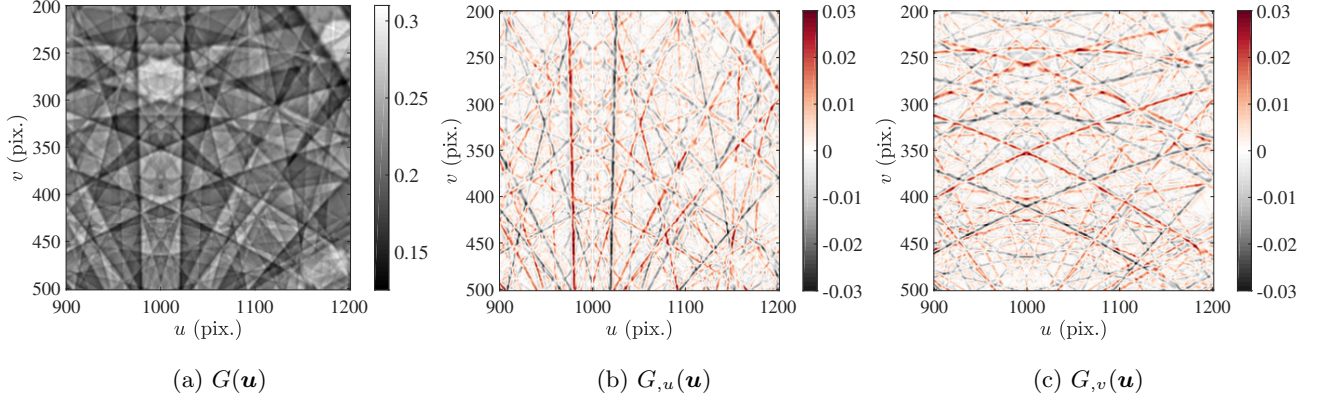


Figure 2: Computation of gradient images. (a) The zoomed master pattern  $G(\mathbf{u})$ . Gradients of the master pattern in direction  $u$  (b) and  $v$  (c).

A slight modification of any parameter  $dP_i$ , induces a modification of the gradients of the simulated image as

$$dg_{,x}(\mathbf{x}) = \left[ \nabla_{\mathbf{u}} G_{,u}(\mathbf{u}) \cdot \frac{\partial \mathbf{u}(\mathbf{x}, \mathbf{P})}{\partial P_i} \frac{\partial u}{\partial x} + \nabla_{\mathbf{u}} G_{,v}(\mathbf{u}) \cdot \frac{\partial \mathbf{u}(\mathbf{x}, \mathbf{P})}{\partial P_i} \frac{\partial v}{\partial x} \right] dP_i \quad (8)$$

$$dg_{,y}(\mathbf{x}) = \left[ \nabla_{\mathbf{u}} G_{,u}(\mathbf{u}) \cdot \frac{\partial \mathbf{u}(\mathbf{x}, \mathbf{P})}{\partial P_i} \frac{\partial u}{\partial y} + \nabla_{\mathbf{u}} G_{,v}(\mathbf{u}) \cdot \frac{\partial \mathbf{u}(\mathbf{x}, \mathbf{P})}{\partial P_i} \frac{\partial v}{\partial y} \right] dP_i \quad (9)$$

The column vector  $\{\delta \mathbf{P}\}$  containing all additive corrections to  $\mathbf{P}$  is obtained

$$[\mathbf{M}] \{\delta \mathbf{P}\} = \{\boldsymbol{\gamma}\} \quad (10)$$

where  $[\mathbf{M}]$  is the Hessian matrix of size  $6 \times 6$  (the degrees of freedom of  $\mathbf{P}$ ) at iteration  $n - 1$

$$M_{ij}^{(n-1)} \equiv \frac{\partial^2 \Theta}{\partial P_i \partial P_j} \quad (11)$$

and the second member  $\{\boldsymbol{\gamma}_i\}$  includes the residual field

$$\gamma_i^{(n)} \equiv \frac{\partial \Theta}{\partial P_i} \quad (12)$$

The explicit expressions of  $[\mathbf{M}]$  and  $\{\boldsymbol{\gamma}_i\}$  can be derived by the chain rule without special difficulties, thus not fully detailed here. Though Equations 11-12 resemble that of Refs.[28, 40, 32], their explicit expressions differ one from another, as the cost functions are different.

When  $\|\{\delta \mathbf{P}\}\| < \epsilon$ ,  $\epsilon$  being chosen equal to  $10^{-6}$  here, the minimization stops and  $\mathbf{P}$  is stored. Otherwise,  $\mathbf{P}$  is updated incrementally

$$\mathbf{P}^{(n)} = \mathbf{P}^{(n-1)} + \delta \mathbf{P}^{(n)} \quad (13)$$

Once  $\mathbf{P}$  is obtained, the gradient images of simulated EBSP resemble the reference experimental EBSP gradients at best.

## 2.2 Example

Figure 3 shows an example of IDIC-G EBSD calibration. Figure 3a shows the full EBSP after Gaussian smoothing, a necessary step to reduce the noise in the gradient image shown in Figures 3c-3d. Dozens of indexed K-bands and their labels are overlapped on Figure 3a, with bands of the same crystal plane families drawn with the same color. The simulated EBSP, by projecting the EMsoft master pattern with the parameters calibrated by IDIC-G, is shown in Figure 3b. Figure 3b also shows the queried points for the gray level profile calculation of the K-band NO.14. The yellow solid line corresponds to the central line of the K-band, or the intersection line of the reflector plane and the EBSD detector. On each side of the central line, 4 hyperbolas are drawn as yellow dashed lines, each being the intersection between a Kossel cone and the EBSD detector. The reflection angle  $\theta$  for the cones form an arithmetic series between 0 and  $2\theta_B$ . The gray levels (GL) of each queried point are obtained by interpolation, and the GL values of each hyperbola are averaged to represent the mean brightness of the K-band with the specific  $\theta$ .

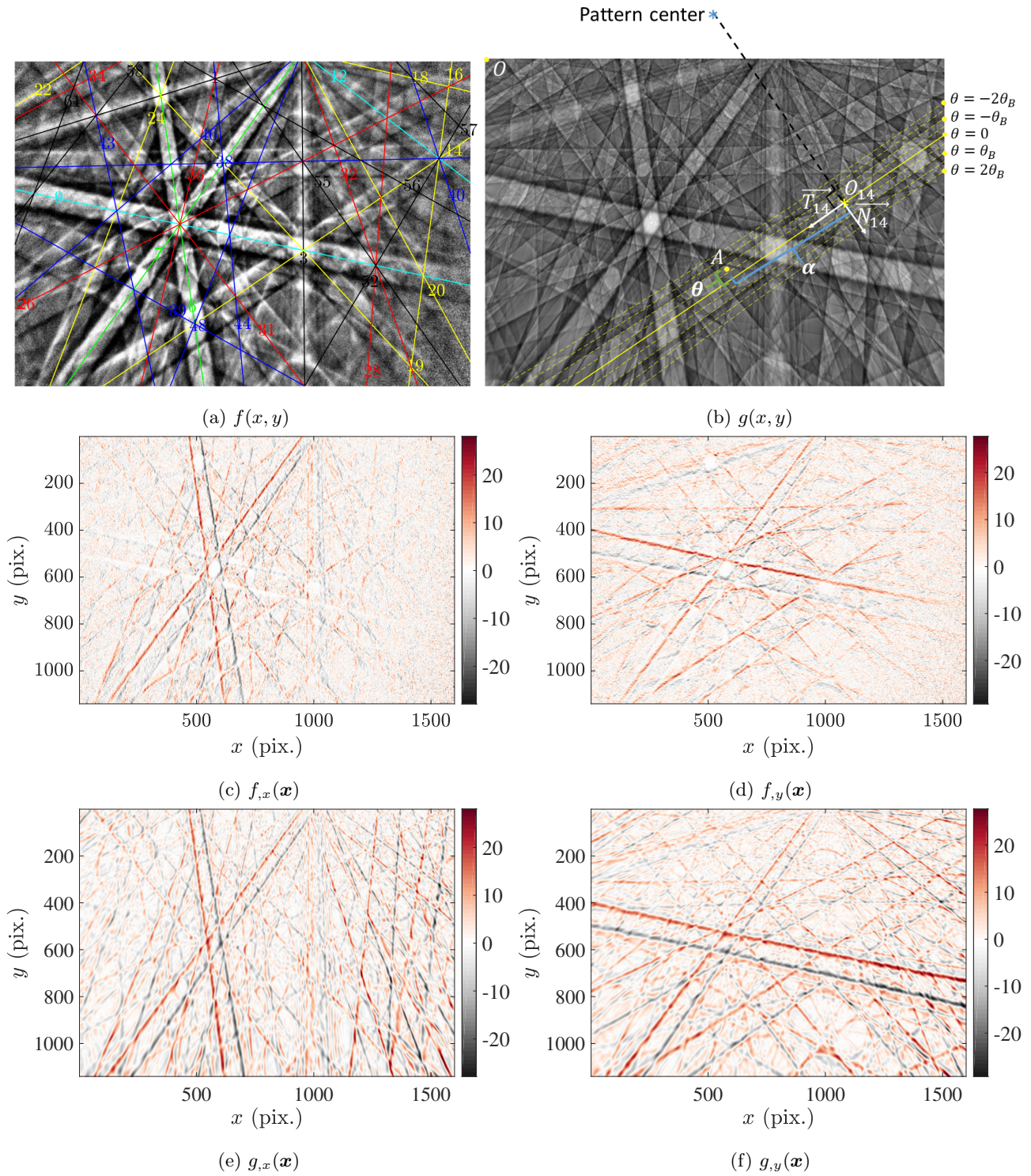


Figure 3: An example of IDIC-G EBSD calibration on EBSD gradients. (a) Experimental EBSD of size  $1140 \times 1600$  of a Si wafer, with dozens of indexed K-bands overlapped; (b) The simulated EBSD by EMsoft with the projection parameters calibrated by IDIC-G. The yellow lines indicate the query points of the K-band NO.14 to obtain the average gray level profile across the band. (c-d) Gradient images in  $x$  and  $y$  directions of (a); (e-f) Gradient images in  $x$  and  $y$  directions of (b).

Positioning of K-bands through the analysis of their profiles is an essential and preliminary step of EBSD analyses varying from crystal orientation indexation to PC calibration and phase identification. K-bands are identified as straight lines by a Hough-transformation, then as parallel circles on a sphere by a 3D Hough transformation [41], or as hyperbolas on the 2D detector. As K-bands intersect each other and modify the gray levels at their crossings, advanced image processing methods such as the use of bandlets [42] have been adopted to precisely locate the K-band edges. Finding these edges is no longer the first step of EBSD analyses when using full pattern match. Nonetheless, the K-band profiles and the geometrically calculated K-band edges from PC can be used to demonstrate the correctness of calibration.

The K-bands corresponding to the highest structure factor reflector planes are analyzed, *i.e.*, 4 (111) planes, 6 (220) planes, 3 (400) planes, 12 (311) planes, 12 (422) planes, 12 (331) planes, and 12 (620) planes. In total, 61 reflector planes are calculated, though they are not all present in each EBSP. Figure 3a plots the existing K-bands in an EBSP, together with their order.

An EBSP can be expressed as the gray level on each pixel  $f(x, y)$ , it can also be viewed as the gray level profiles of numerous K-bands  $\mathcal{F}(b, \theta)$  as illustrated in Figure 3b. The coordinate of a point  $A$  in the proximity of band NO. $b$  can be expressed as:

$$\overrightarrow{OA} = \overrightarrow{OO_b} + \alpha \overrightarrow{T_b} + \theta \overrightarrow{N_b} \quad (14)$$

where  $\overrightarrow{T_b}$  is a unit vector in the  $(x, y)$  plane parallel with the diffracting plane NO. $b$ , and  $\overrightarrow{N_b}$  a unit vector vertical to the same diffracting plane as shown in Figure 3b. The average gray level over  $\alpha$  of points with constant  $(b, \theta)$  is hence defined as the average band profile of an EBSP. The average band profile for the experimental and simulated EBSPs are denoted  $\mathcal{F}(b, \theta)$  and  $\mathcal{G}(b, \theta)$  respectively.

Figure 4 shows the average band level profiles, expressed in the space of  $(b, \tilde{\theta})$ , of the K-bands of Figure 3a-3b. The green dashed lines highlight the calibrated K-band edges. For most K-bands,  $\mathcal{F}(b, \theta/\theta_B)$  is not symmetrical, as the gray level is higher for upper edge (left side of Figure 4a), while  $\mathcal{G}(b, \theta/\theta_B)$  is very symmetrical. This excess-deficit effect influences the full pattern match of experimental and simulated EBSPs, both in the space of  $(x, y)$  and of  $(b, \theta)$ .

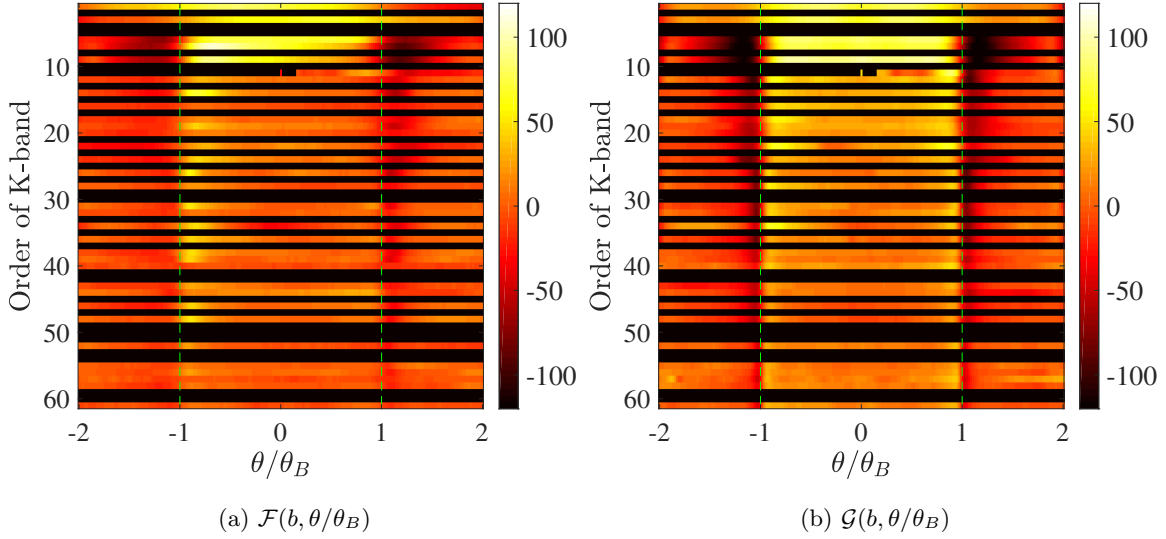


Figure 4: Average band profiles computed from Fig. 3a (a) and Fig.3b (b).

The cross-correlation function (XCF) of  $\mathcal{F}(b, \theta/\theta_B)$  and  $\mathcal{G}(b, \theta/\theta_B)$ , as defined in Equation 15, shows the match result of gray level profiles of each K-band. The XCF of the gradients of gray level profiles,  $\text{XCF}_\theta(b, \tau)$ , is defined in Equation 16, where  $\mathcal{F}_\theta(b, \tau - \theta)$  stands for the gradient of  $\mathcal{F}(b, \tau - \theta)$  along direction  $\theta$ .

$$\text{XCF}(b, \tau) = \sum_{\theta} \mathcal{F}(b, \theta - \tau) \mathcal{G}(b, \theta) \quad (15)$$

$$\text{XCF}_\theta(b, \tau) = \sum_{\theta} \mathcal{F}_\theta(b, \theta - \tau) \mathcal{G}_\theta(b, \theta) \quad (16)$$

The analyses of gray level profiles are provided in Figure 5. Figure 5a plots the average gray level profiles of the K-band NO.3 for the experimental and simulated patterns, together with their gradients across the K-band. This band is almost vertical, thus the excess-deficiency effect is negligible. Besides, this band belongs to the (111) diffracting plane, and the GL variation at the band edge is very smooth. The cross-correlation (XCF) profile between the experimental and simulated GL profiles, together with the XCF of the GL gradient profiles, are shown in Figure 5b. The two XCF curves peak at the same position  $\theta = 0$ , indicating that there is no shift effect between the full EBSP and its gradients for this vertical band. Figure 5c-5d show the same plots for the K-band NO.14 of the diffracting plane family (311). This band is inclined at  $55^\circ$  from the vertical direction, and the excess-deficiency effect is highly visible in the experimental pattern shown in Figure 3a and in the GL profile in Figure 5c. For the simulated EBSP, no excess-deficiency effect is present, and the GL profile is close to symmetry. The GL contrast for band NO.14 is high at the band edge, where the GL gradient reaches extreme values. Importantly, despite the significant excess-deficiency effect, the extreme values of the GL gradient profile appear at the same position for experimental and simulated bands. This phenomenon was first observed by Saowadee *et al.* [37] and confirmed by Nolze *et al.* [38]. The XCF profiles of the GL and GL gradient for band NO.14 are shown in Figure 5d. The XCF of GL gradient still peaks at  $\theta = 0$ , showing an appreciable consistency with the K-band NO.3. However, the XCF curve of GL peaks at  $\theta = -0.06 \theta_B$ , indicating that the full pattern match based on the K-band NO.14 tend to be

shifted toward the up-left direction for a distance corresponding to  $0.06 \theta_B$ . Every non-vertical K-band in EBSP is prone to the ED effect, and their combination will induce systematic errors on the calibrated PC coordinates and the crystal orientation.

The two previous examples are illustrative. Figure 5e shows the histogram of the XCF peak position for all the above-enumerated bands, weighted by the length of each K-band expressed in pixels in the EBSP. This statistical study shows that the XCF peak positions, calculated with the GL of K-bands, are centered around  $\langle \theta \rangle = -0.04 \theta_B$ , while those calculated with the GL gradients of K-bands do not show any bias  $\langle \theta \rangle = 0$  and with halved dispersion (standard deviation). This demonstrates the superiority of using the gradients image instead of the full EBSPs. Knowing that the gradient along  $\theta$  can be decomposed on the gradients along  $x$  and  $y$ , this calibration enhancement is also valid for the IDIC-G algorithm. Three experimental datasets are employed in the following to confirm this observation.

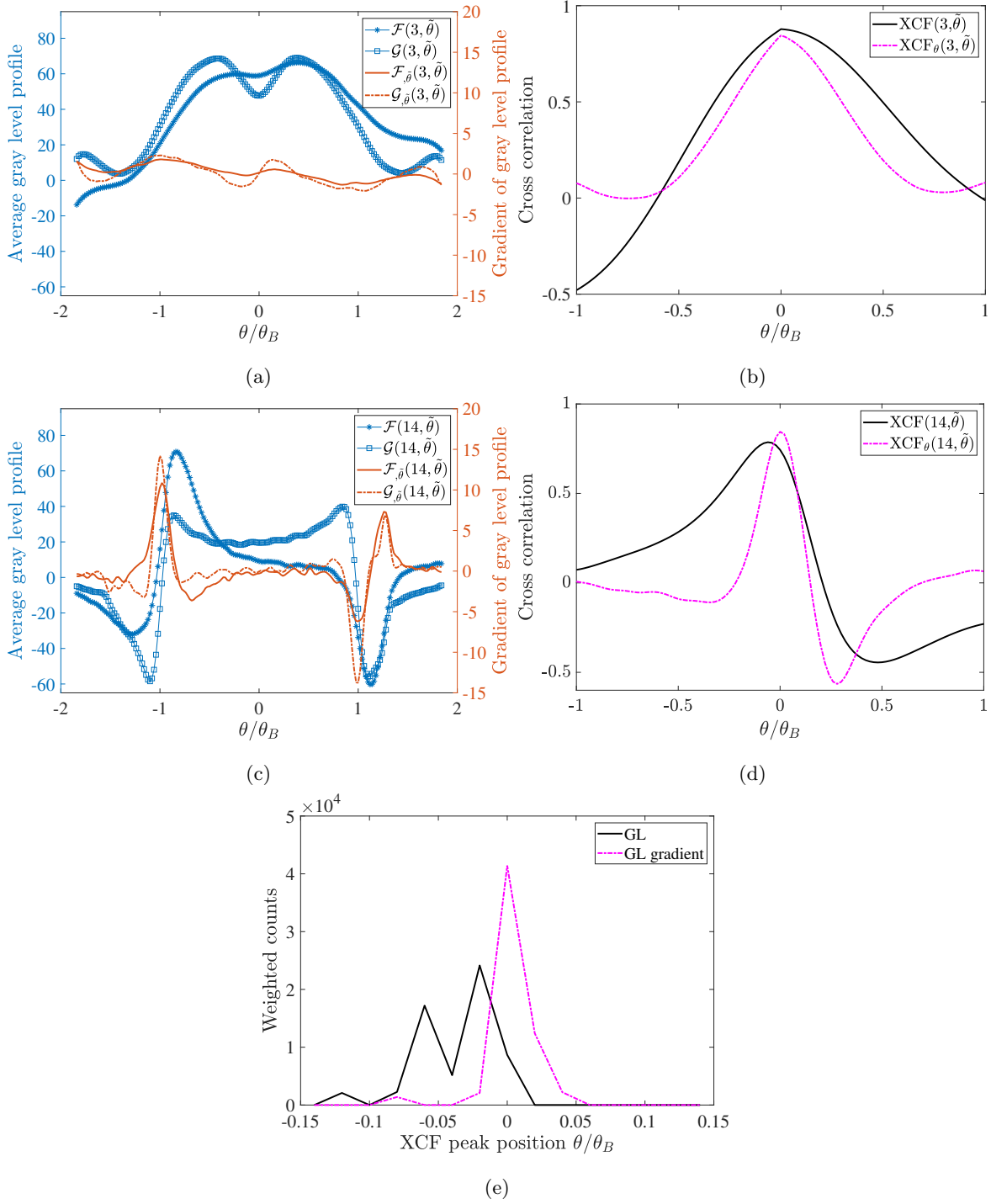


Figure 5: Analysis of gray level profiles in 2 K-bands. (a) Average gray level profiles and their gradients, for K-band NO.3 of the experimental and simulated EBSPs. (b) The cross-correlation values for the gray level profile and its gradient. (c-d) plot the same curves for K-band 14. (e) plots the histogram of the XCF peak position for all the enumerated bands, weighted by the length of each K-band expressed in pixels in the EBSP.

### 3 Comparison with hardware-based EBSD calibration

An experiment was performed to test the proposed EBSD calibration method on an Austenite-Ferrite CF8M steel. The sample is mechanically and electrically polished to prepare for the EBSD acquisition. High definition ( $2048 \times 2048$  pixels) diffraction patterns recorded by Nordiff HR4M EBSD detector are analyzed to provide a  $301 \times 301$  map of crystalline orientation, resolved at a step size of  $1 \mu\text{m}$ . The acceleration voltage is 30kV. The probe current was 60 nA, and the dwell time was 0.6 s. The inverse pole figure for the dual-phase steel is shown in Figure 6a. The thin longitudinal grains are the ferritic matrix (even if only about 20% in volume), and the rest is the austenite transformed from the ferrite during the cooling process [43]. An example of the EBSP of austenite is shown in Figure 6b, where the circular shape denotes the shadow cast by the nose cone. This shadow helps to calibrate the projection center coordinates [44, 17] using the software CrossCourt 4. The pixels outside the circular shape are assigned a zero-weight in both IDIC and IDIC-G computations.

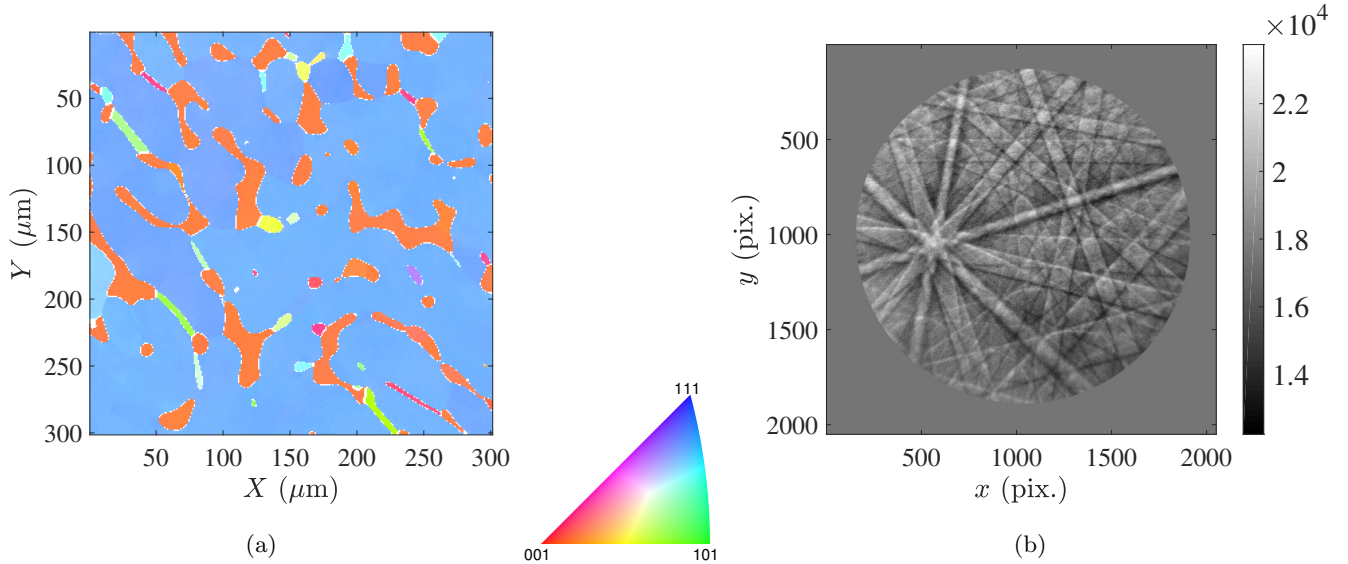


Figure 6: (a) The inverse pole figure of the dual-phase steel. (b) An EBSP of the austenite. The circular shape is due to the nose-cone adopted in the detector to calibrate the projection center.

The shadow-based nose cone calibration method is applied on the patterns, together with the IDIC and IDIC-G algorithms. The PC calibration results obtained by the 3 methods are shown in Figure 7. The ferritic matrix is exposed to more strains and orientation gradients, thus their PC calibration by IDIC and IDIC-G is less precise (than the austenite matrix) and are not compared with the hardware calibration. All 3 calibration methods are able to detect the global variation of PC coordinates. The nose-cone calibration exhibits no discontinuity at the grain boundaries, showing a good neutrality of the crystal orientation and the strain state. On the contrary, IDIC calibration results reveal clearly the grain shapes, showing the necessity of PC discontinuity reduction, but also the potential of strain extraction. Figure 8 compares the differences between shadow-based and IDIC(-G) EBSD calibration results. A distance of about 3-4 pixels exists for all 3 components of PC, which is a good cross-validation of the hardware and software calibration methods, given the size of the EBSP ( $2048 \times 2048$ ). IDIC-G leads to more homogeneous results than IDIC, and lower discrepancy with the nose cone method.

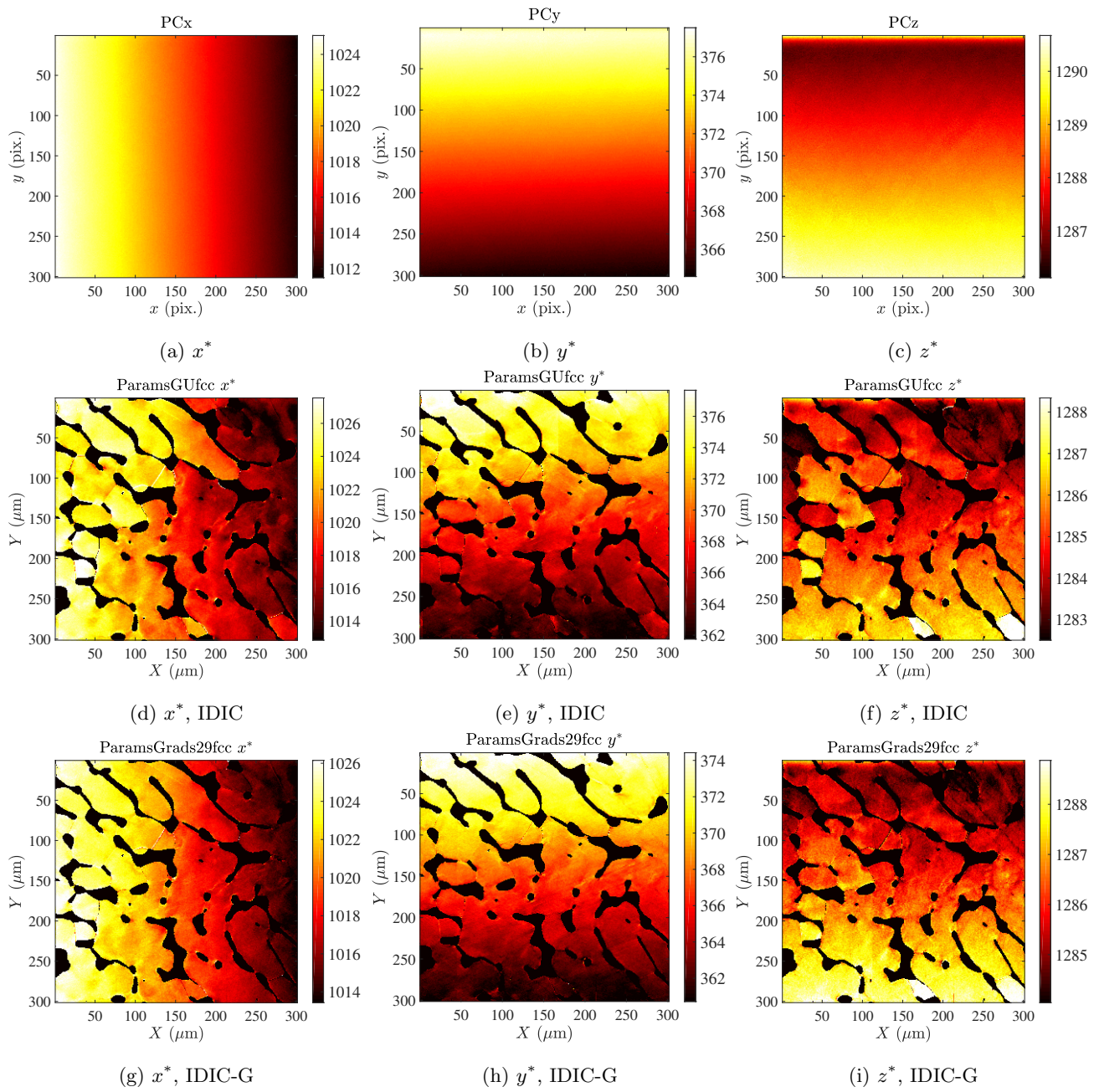


Figure 7: Projection center calibration results. (a-c) Shadow by nose cone. (d-f) IDIC with full EBSP patterns. (g-i) IDIC-G with EBSP gradients.

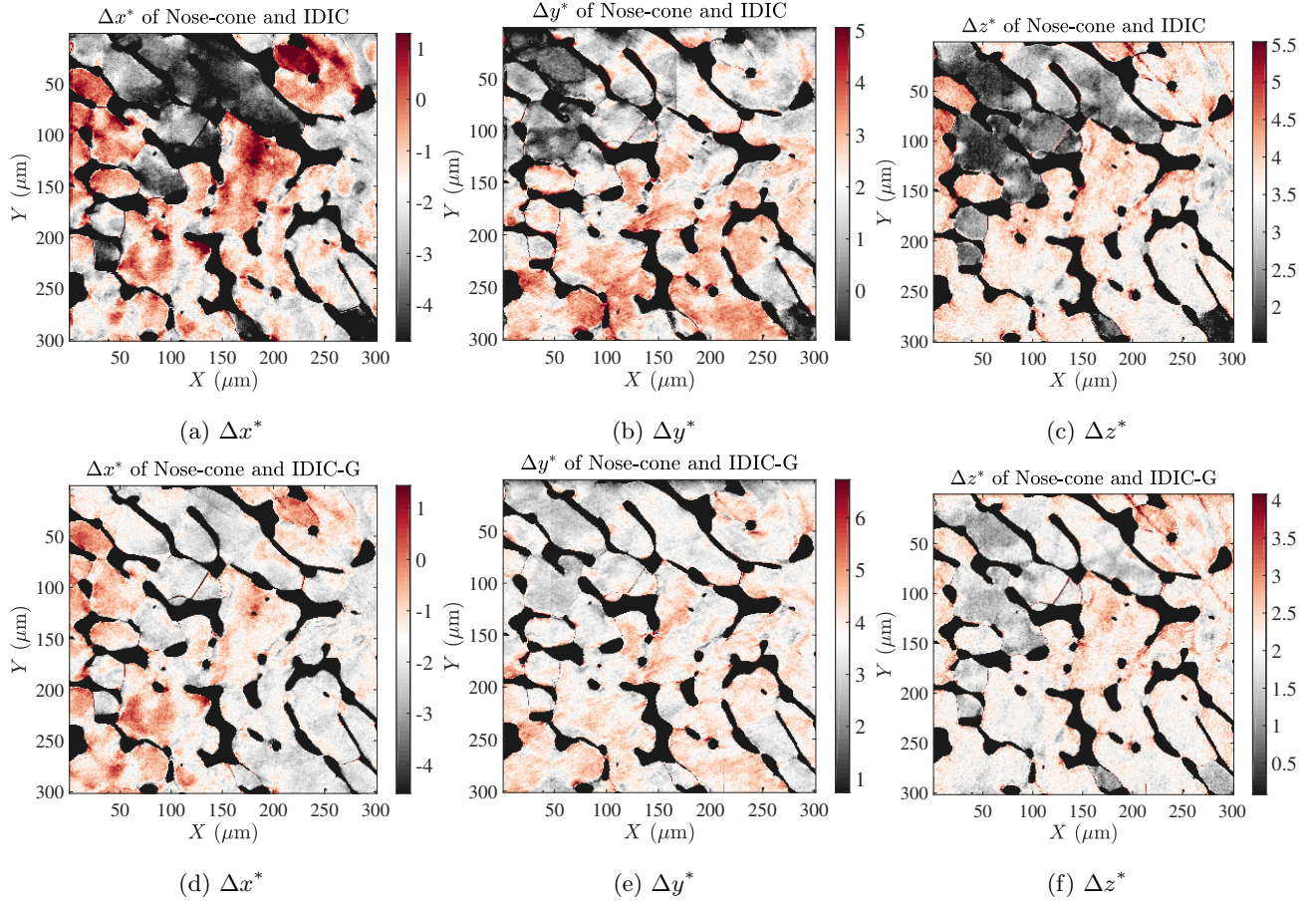


Figure 8: Difference between shadow-based (nose cone method) calibration and full pattern match calibration results. (a-c) PC coordinates differences between shadow-based and IDIC results. (d-f) PC coordinates differences between shadow-based and IDIC-G results.

Figure 9a shows the histogram of  $\delta \mathbf{x}$ , PC deviations to their linear fitting, calibrated by IDIC and IDIC-G algorithms. For all 3 components, IDIC-G leads to a 40-50% reduction of deviations, which is also visible in Figure 8. Figure 9b plots the distribution of KAM values indexed by IDIC and IDIC-G. For this unstrained sample, the KAM indexed by IDIC-G is on average  $0.01^\circ$  smaller than IDIC. As a result, IDIC-G outperforms IDIC both in orientation indexation uncertainty and PC calibration.

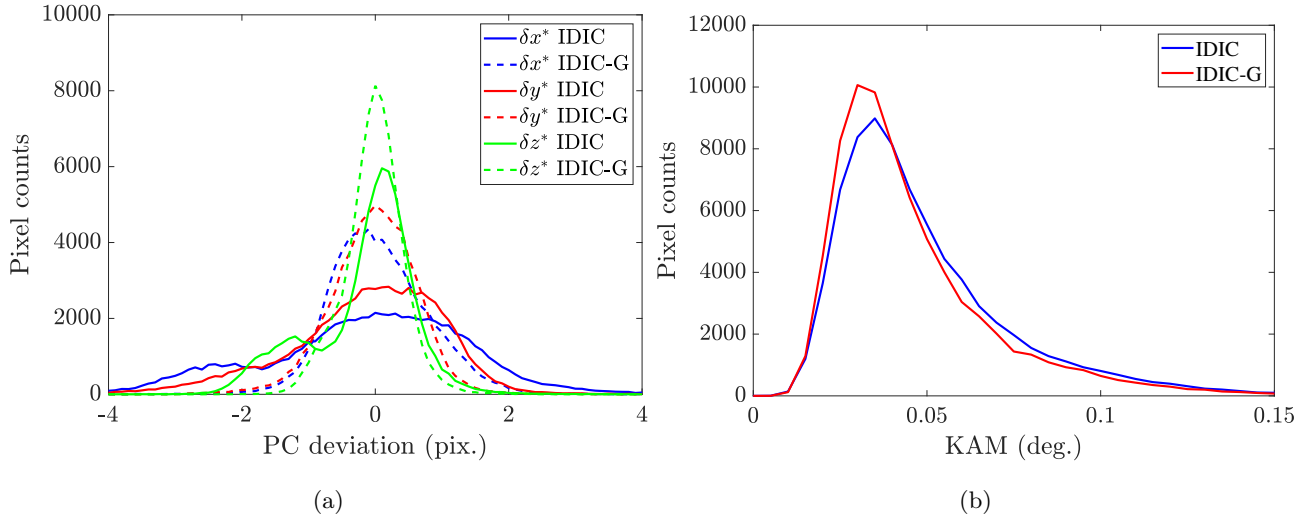


Figure 9: Performance comparison of IDIC and IDIC-G EBSD calibration. (a) PC coordinate deviations. (b) Kernel average misorientation distributions.

## 4 Test on unstrained polycrystal EBSD acquisitions

An experiment was performed to test the proposed EBSD calibration method on an Al-Mg alloy (6 wt.% Mg), which is detailed in Refs. [45, 28]. The sample is mechanically polished and chemically etched to prepare for the EBSD acquisition. High definition ( $1200 \times 1600$  pixels) diffraction patterns recorded by Bruker *e-Flash<sup>HD</sup>* EBSD detector are analyzed to provide a  $30 \times 40$  map of crystalline orientation at a step size of  $3.43 \mu\text{m}$ . The acceleration voltage is 20kV. The probe current was 20 nA, and the dwell time 0.9 s. A series of EBSD has been acquired with different sample tilt angles ( $70^\circ$ ,  $65^\circ$  and  $60^\circ$ ) on the same sample area, in order to demonstrate the performance of the calibration algorithms on different tilt angles.

Figures 10a-10c show the EBSPs of the same grain acquired with different sample tilt angles, where the indexed K-bands are overlapped. A significant shift exists between the 3 EBSPs, and the image quality deteriorates as the tilt angle passes from  $70^\circ$  to  $60^\circ$ . Figure 10d shows the inverse pole figure of the scanned area. Figure 10e plots the weighting factor  $\omega(\boldsymbol{x})$  for the  $70^\circ$ -tilt dataset, which is calculated as the reverse of the noise level at different EBSP parts.

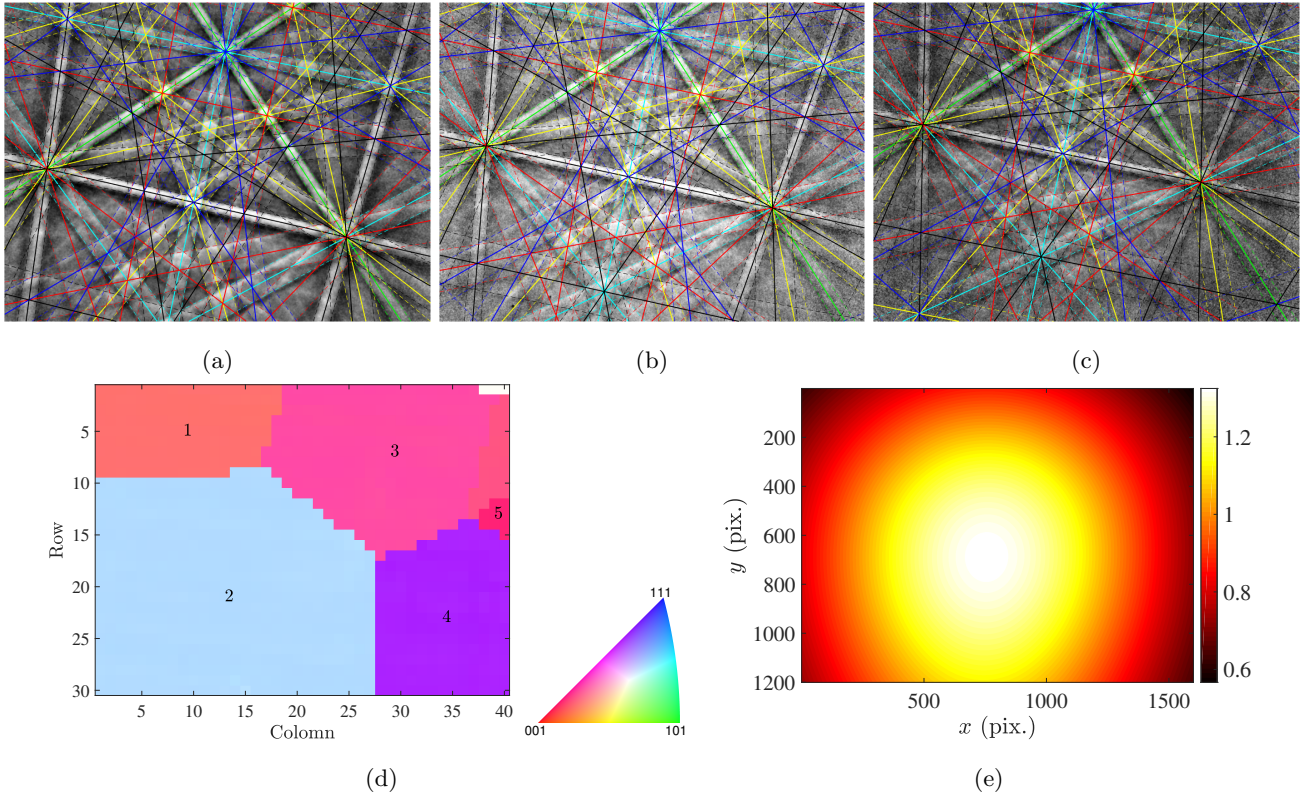


Figure 10: (a-c) EBSD of the same position with sample tilt  $70^\circ$ ,  $65^\circ$  and  $60^\circ$  respectively. (d) Inverse pole figure of the polycrystal. (e) The weighting factor  $\omega(x, y)$  for sample tilt  $70^\circ$ .

The three EBSD scans, each including 1200 EBSDs, are calibrated by IDIC and IDIC-G EBSD methods.

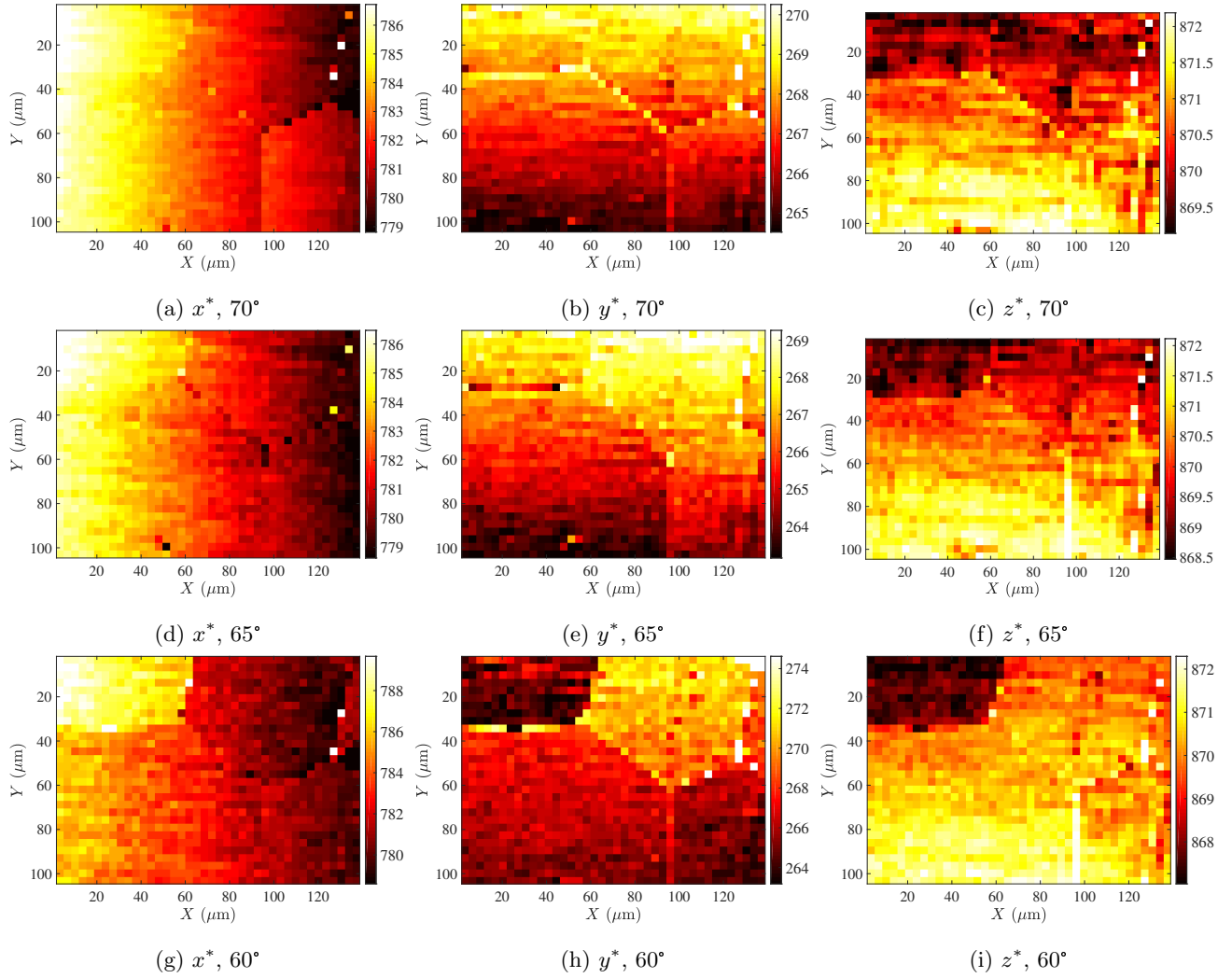


Figure 11: Calibrated pattern center components  $x^*$ ,  $y^*$  and  $z^*$  (in pix.) for the AlMg alloy for sample tilt angles  $70^\circ$ ,  $65^\circ$ , and  $60^\circ$ . The full EBSPs are used for IDIC calibration.

Figure 11 shows the calibrated pattern center fields for each EBSP and different sample tilt angles while taking the full EBSPs in the calibration. Discontinuities in the PC fields at grain boundaries are readily visible, especially for the case of  $60^\circ$ . The bad performance of EBSD analyses in the latter case is mainly due to the anomalous K-band gray level distribution. When the tilt angle is lower than the standard  $70^\circ$ , the lower part of the EBSP often displays negative gray level variations inside the K-bands [31].

Figure 12 shows the calibrated PC fields for different sample tilt angles based on the EBSPs *gradient*. PC field discontinuities at grain boundaries have been significantly reduced. Besides, the  $y^*$  value has on average increased by about 1 pixel with IDIC-G.

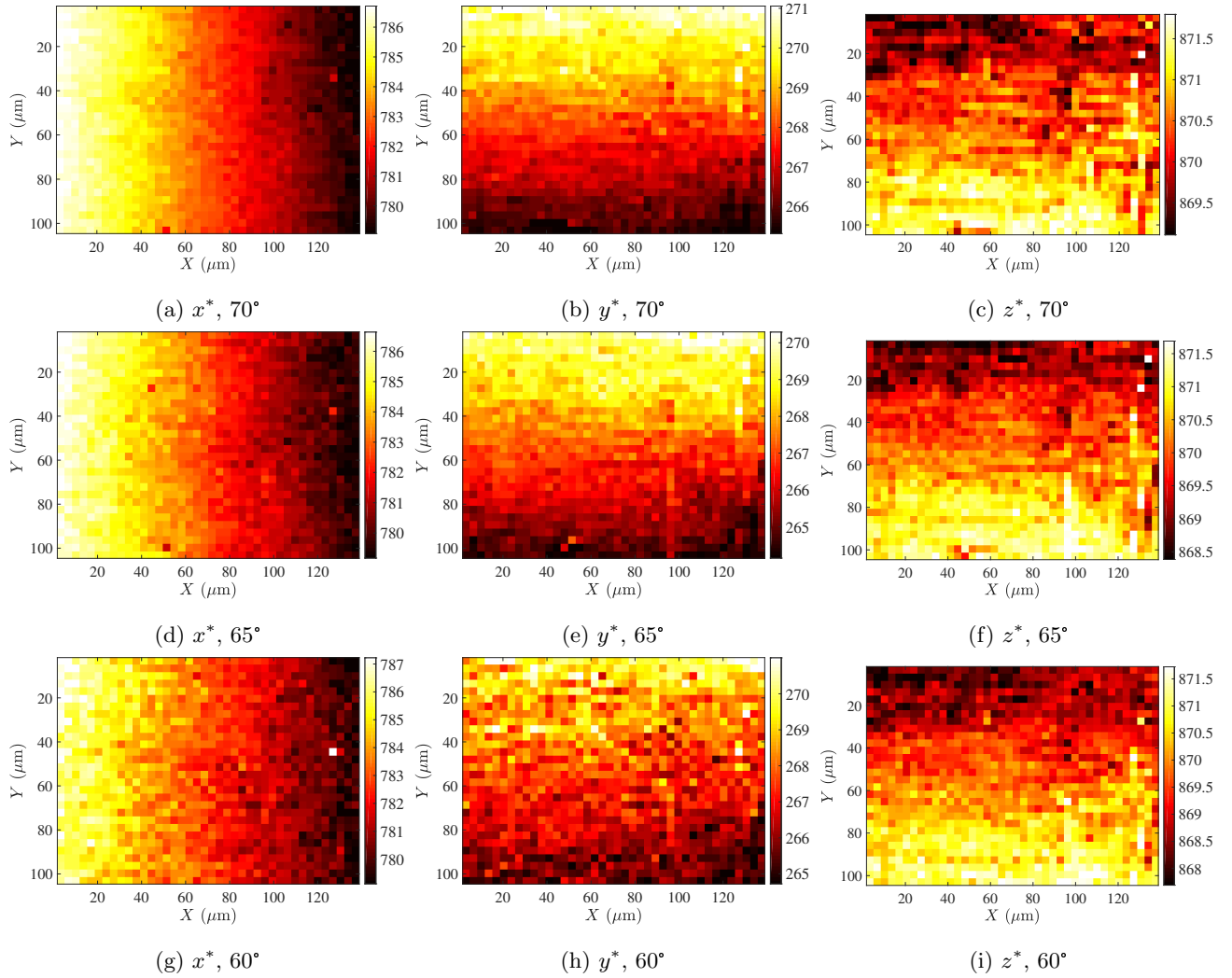


Figure 12: Calibrated pattern center components  $x^*$ ,  $y^*$  and  $z^*$  (in pix.) for the AlMg alloy for sample tilt angles  $70^\circ$ ,  $65^\circ$ , and  $60^\circ$ . EBSPs gradients are used for calibration (IDIC-G EBSD).

Figure 13 shows the change of calibrated PC fields between IDIC-G and IDIC. The changes of  $x^*$  and  $z^*$  values when taking image gradients are various, while  $y^*$  value increases between 1-2 pixels for most grains. The two top grains (No. 1 & 3) of sample tilt  $60^\circ$  are exceptions, as their IDIC calibration results are less accurate. This is an evidence that to accommodate the ED phenomenon, simulated EBSPs tend to shift upwards thus the calibrated  $y^*$  is systematically lower than the true value. We believe all the previous FPM-based EBSD calibration methods suffer from this drawback, regardless of the adopted optimization method [27, 29, 25, 46, 28]. By resorting to a simple gradient, the gray level asymmetry is largely reduced, and the overall systematic underestimation of  $y^*$  is cancelled. The highly-demanding simulation of ED effect is thus avoided, and the computation cost of the calibration is very low.

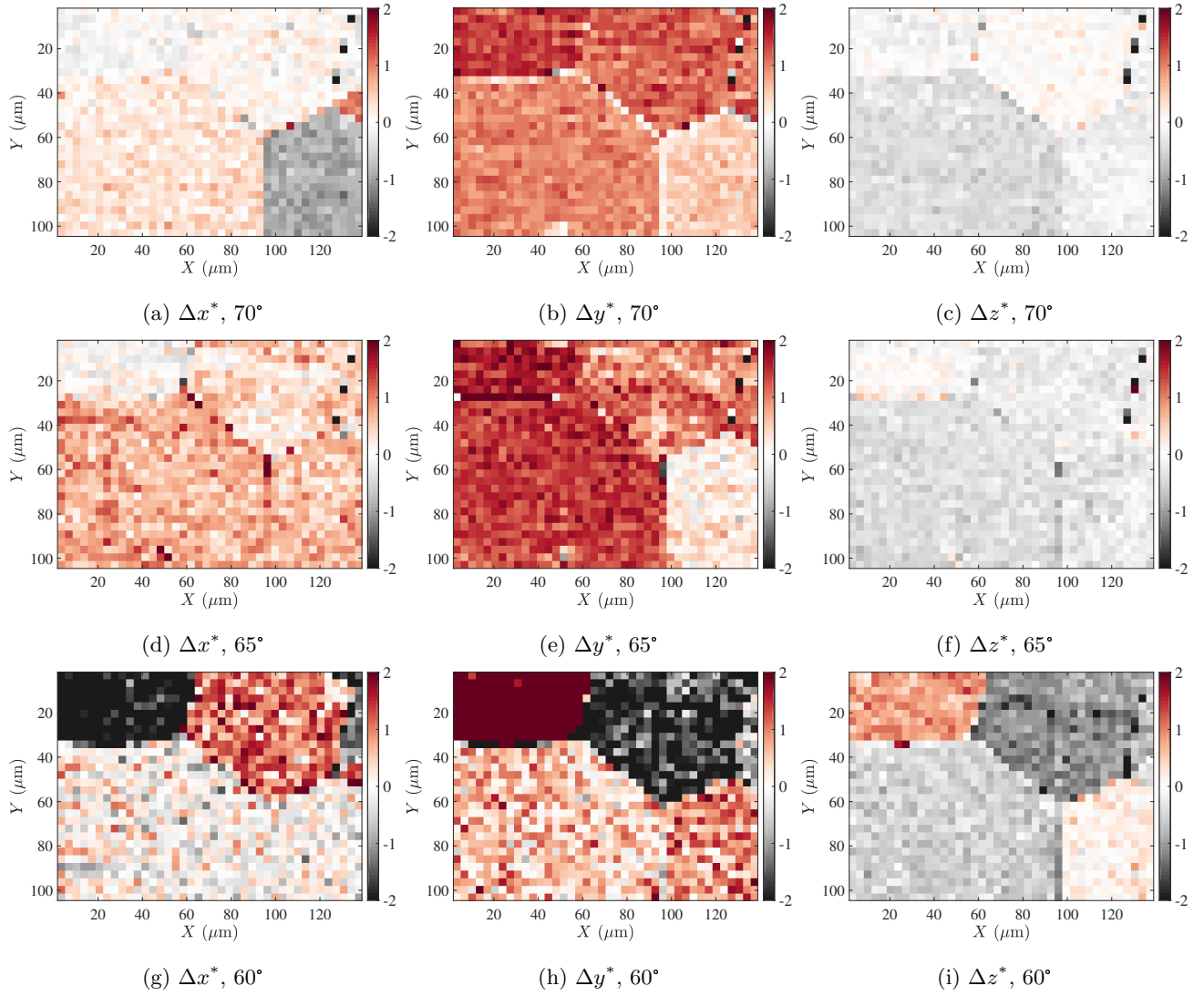


Figure 13: PC variation between IDIC and IDIC-G calibration for sample tilt  $70^\circ$ (a-c),  $65^\circ$  (d-f) and  $60^\circ$ (g-i) respectively.

Figure 14 shows  $\delta \mathbf{x}$ , the deviation of PC components from their linear fitting for different tilt angles. IDIC-G improves the PC continuity significantly at grain boundaries, with the statistics summarized in Table 2.

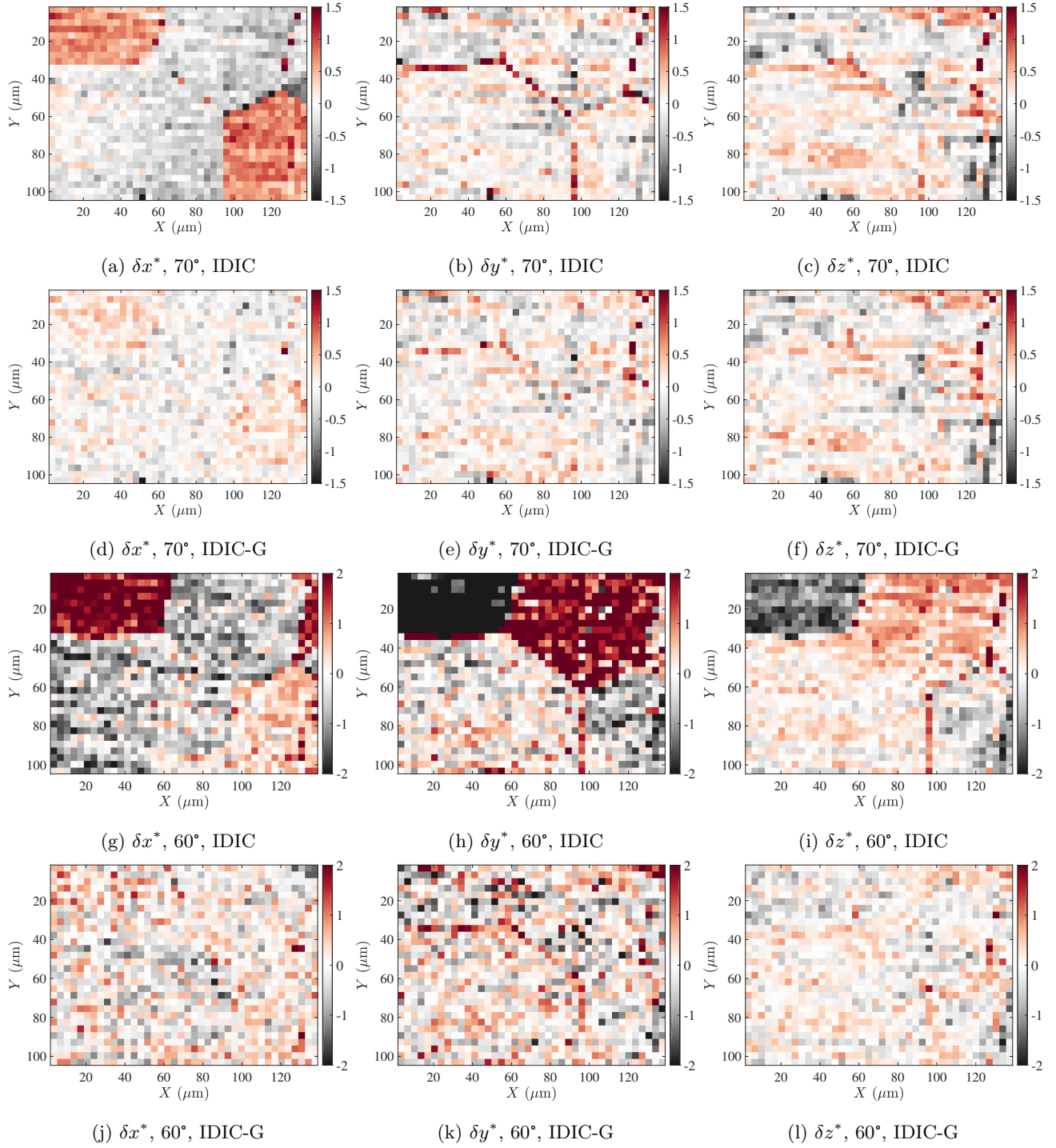


Figure 14: Deviation from linearity of PC components  $x^*$ ,  $y^*$  and  $z^*$  (in pix.), calibrated by IDIC and IDIC-G for sample tilt angles of 60° and 70°.

## 5 Test on a 10% strained polycrystal sample

An experiment was performed to test IDIC-G method on a strained Al-Mg alloy (6 wt.% Mg), which is detailed in Ref. [40]. The sample is cold rolled to a 10% reduction of thickness, then mechanically polished and chemically

etched to prepare for the EBSD acquisition. High definition ( $1200 \times 1600$  pixels) diffraction patterns recorded by Bruker  $e^- Flash^{HD}$  EBSD detector are analyzed to provide a  $150 \times 200$  map of crystalline orientation, resolved at a step size of  $6.87 \mu\text{m}$ . The acceleration voltage is  $20\text{kV}$ . The probe current was  $20 \text{ nA}$ , and the dwell time was  $0.9 \text{ s}$ .

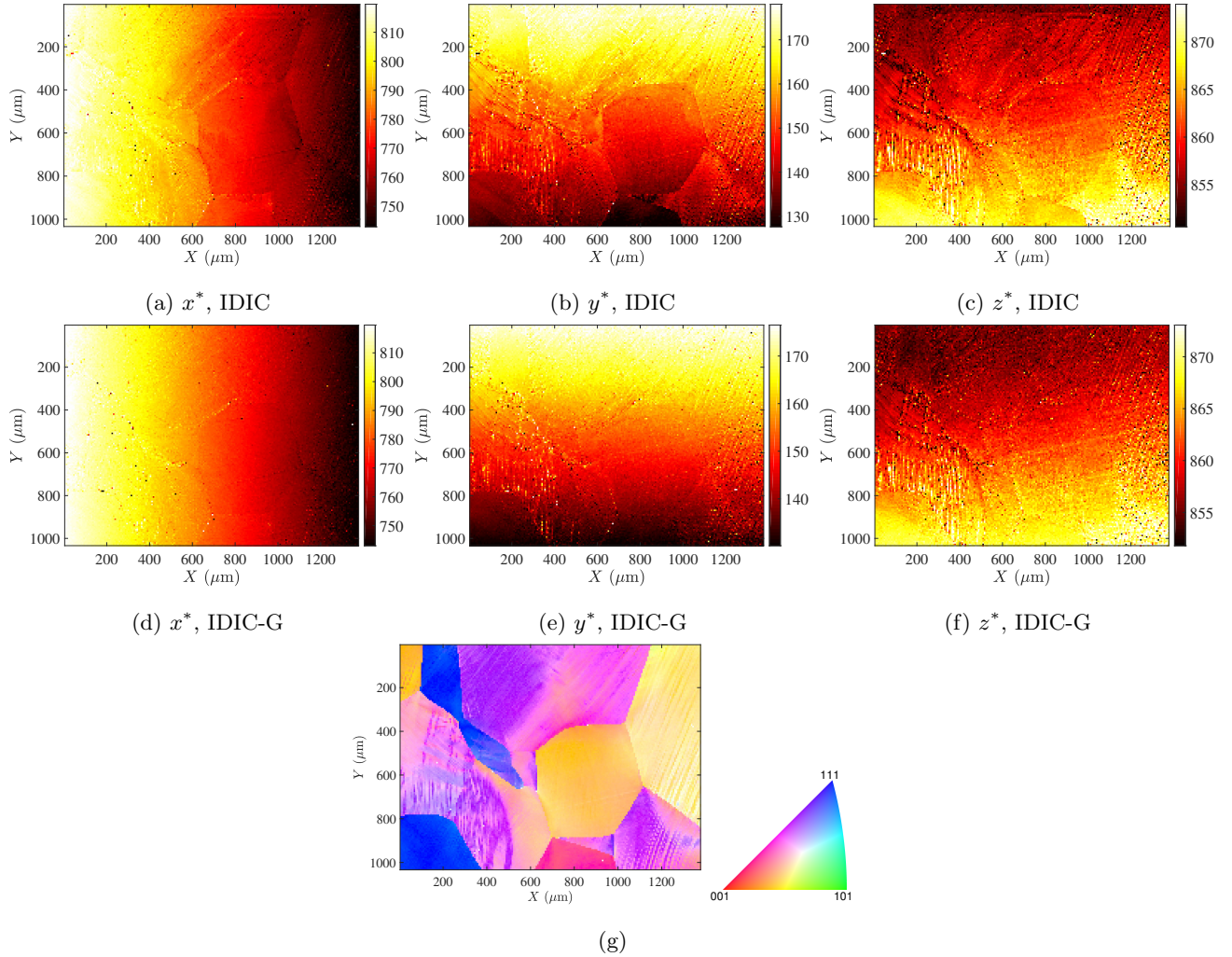


Figure 15: Calibrated pattern center components  $x^*$ ,  $y^*$  and  $z^*$  (in pix.) for the cold rolled AlMg alloy, calculated by IDIC calibration (with full EBSPs) and IDIC-G calibration (with gradients of EBSPs). (g) Inverse pole figure of the cold rolled polycrystal.

Figures 15a-15f show the calibrated projection center coordinates for each EBSP obtained with IDIC and IDIC-G respectively, while the inverse pole figure of the cold-rolled Al-Mg sample is given in Figure 15g. PC field discontinuities at grain boundaries are readily visible for IDIC, and they have been significantly reduced for IDIC-G. The deviation of the PC point cloud to its plane fit,  $\delta x^*$ ,  $\delta y^*$  and  $\delta z^*$ , are shown in Figure 16 for both algorithms. The PC deviations for IDIC-G are reduced by 38% as compared to those of plain IDIC. This test case demonstrates the enhanced performance of IDIC-G over IDIC on strained samples.

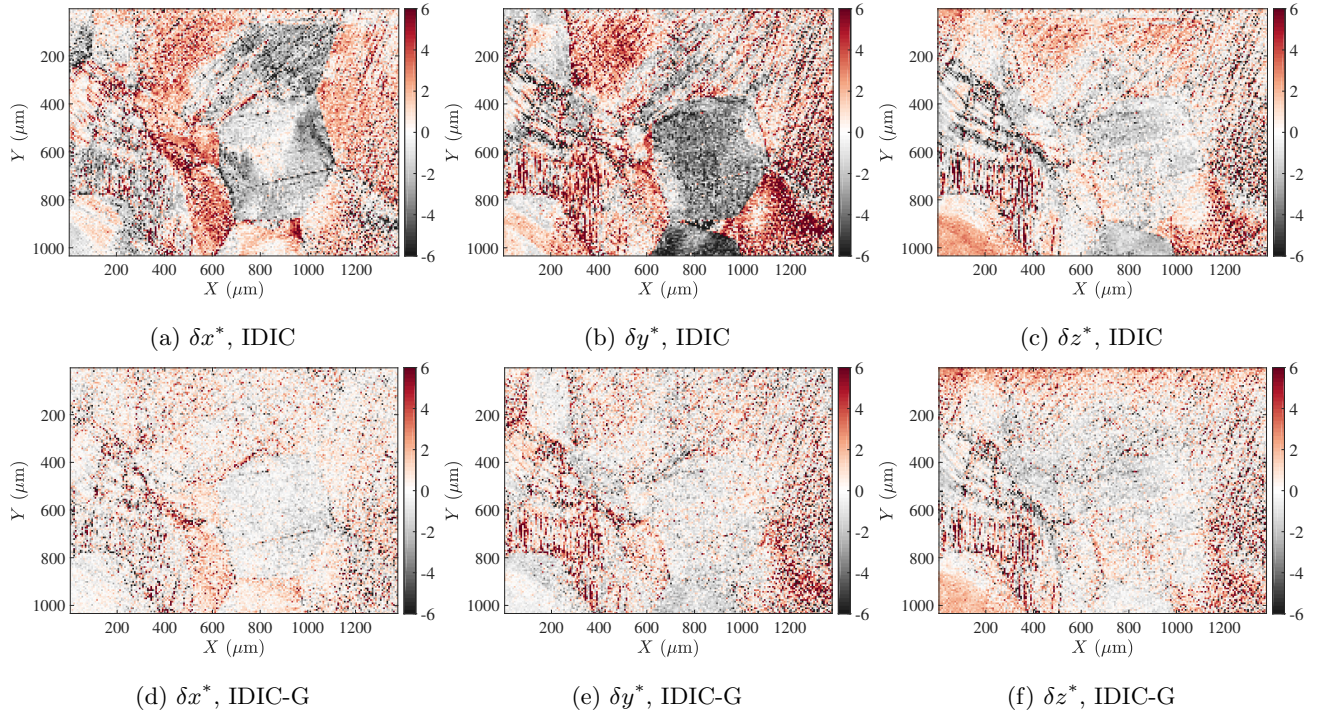


Figure 16: The derivation from the linearly fitted PC components of Calibrated pattern center components  $\delta x^*$ ,  $\delta y^*$  and  $\delta z^*$  (in pix.) for IDIC and IDIC-G results.

Table 2: Summary of calibration performance of IDIC or IDIC-G EBSD for the polycrystal Al-Mg alloy

Algorithm	IDIC				IDIC-G			
	Scanned area (mm <sup>2</sup> )	1.0×1.4	0.10×0.14		1.0×1.4	0.10×0.14		
Strain state	10% rolled	Unstrained			10% rolled	Unstrained		
Tilt angle (°) setup	70	70	65	60	70	70	65	60
Tilt angle (°) fitted by PC	72.6	68.4	64.3	83.8	71.8	72.0	67.4	60.0
Median distance to planar fitting (pix.)	1.62	0.462	0.469	1.08	1.20	0.429	0.461	0.672
Median deviation of PC (pix.)	3.40	0.603	0.605	1.44	2.00	0.419	0.529	0.819
Computing time (s) per EBSP	35	28	41	80	68	54	95	117

The performance of IDIC EBSD calibration is summarized in Table 2. A plane fitting as described in Ref. [47] is applied on each PC calibration result, and the sample tilt angle is estimated. IDIC-G PC data consistently overestimate the tilt angle by about 2°, except for the 60° scan. This result implies a tilt angle of 2° of the EBSD detector. The tilt angles predicted by IDIC PC data are more dispersed, showing the better calibration accuracy of IDIC-G. Besides, the tilt angles predicted by IDIC and IDIC-G PC data are closest for the large-area scan (1.0×1.4mm<sup>2</sup>) among the 4 datasets, despite its strain. This phenomenon shows that a large scan area helps to

calibrate the sample position more precisely. The distance of PC points cloud to its plane fit is also provided, with a smaller distance indicating a better PC estimation. Compared to IDIC calibration, IDIC-G reduces the distance to plane fitting and the deviation of PC components to their linear fitting, with an improvement up to 45%. The proposed gradient filter on EBSPs could reduce the systematic errors in calibration results, for which the improved PC continuity at grain boundaries and the improved plane fitting of PC fields are firm indications.

The computing time for each EBSP is also provided, tested in Matlab installed on a Dell laptop with CPU i7-10750H. The computing time increases gradually when the sample tilt passes from 70° to 65° and 60°, as the band features dwindle and the noise level amplifies (see Figure 10). Besides, the computing time of each EBSP by IDIC-G is close to twice as much as that by IDIC. This is due to image interpolation, which is the most time-consuming step, and is performed twice per iteration for IDIC-G as compared to once for IDIC. Note that this additional time cost is negligible when compared with the full dynamical simulation considering the excess-deficit effect [35].

The proposed gradient filter on EBSPs could reduce the systematic errors in calibration results, for which the improved PC continuity at grain boundaries and the improved similitude with hardware calibration results are firm indications. As the crystal orientation indexation and PC calibration are closely intertwined in FPM methods, IDIC-G is expected to improve the orientation indexation, especially in the reduction of systematic errors.

Both IDIC-G and IDIC are applied to several other datasets with varying pattern sizes and qualities, which are not detailed here for brevity. Let us emphasize that IDIC-G improves both *accuracy* and *uncertainty* only on medium-to-high-resolution ( $\geq 240 \times 320$ ) high-quality EBSPs. For medium-to-high-resolution low-quality EBSPs, IDIC-G reduces the systematic errors yet increases the random error in PC calibration. For smaller EBSPs ( $\leq 120 \times 160$ ) of lower quality, the noise increment in the gradient operation is severe and IDIC-G EBSD results in high indexation uncertainty. As a result, it is suggested to conduct IDIC-G on medium-to-high-resolution EBSPs, especially when the excess-deficiency effect is important, and adopt IDIC on low-resolution EBSPs.

## 6 Conclusion

Full pattern match with simulated diffraction pattern has drawn increasing attention in advanced EBSD analyses, mainly thanks to its high precision and little constraints. Some aspects of experimental EBSPs are however difficult or costly to simulate, such as Kikuchi band brightness asymmetry, gray level reversal for small tilt angles and non uniform diffracted electron energy. This paper proposes to overcome the K-band asymmetry by integrated digital image correlation with gradient operations (IDIC-G) on EBSPs. The excess-deficit phenomenon of K-band gray level, *i.e.*, brighter upper-edge and darker lower-edge, induces systematic errors and uncertainties for IDIC, and these difficulties are essentially mitigated by correlating the gradients instead of the full diffraction patterns, at the price of doubling the calibration time cost.

Through 3 tests on high-resolution EBSPs, the IDIC-G method has been shown to improve the EBSD calibration compared to IDIC on the full EBSPs. The projection center continuity across grain boundaries improves by 50%, for unstrained and strained samples, and for various sample tilt angles. The analysis of average gray level profiles shows that IDIC-G predicts the K-band positions also with a 50% improvement compared with IDIC on full EBSPs. Besides, IDIC-G calibration results, rather than the full EBSP images, leads to a closer result to the

hardware calibration method. Failing to account for the K-band asymmetry effect will deviate the PC from true value by 1-2 pixels, especially for  $y^*$  where the excess-deficiency phenomenon mainly exists. The crystal orientation *uncertainty* also improves by  $0.01^\circ$  by IDIC-G as demonstrated in the steel dataset.

The proposed gradient operation to mitigate the K-band asymmetry effect is suggested to be used for all EBSD analyses based on experimental and simulated EBSP correlation, such as strain estimation, tetragonality mapping and lattice constant refinement. Besides, the gradient operation could also be extended to several other types of diffraction images. For example, TKD has a more expressed K-band asymmetry due to its higher acceleration voltage, and better analysis results are expected when resorting to EBSP gradients.

## Acknowledgements

This work is financially supported by the National Key Research and Development Program of China, 2021YFA1600900, and National Natural Science Foundation of China [No. 52273229, 51901132]. We are also grateful to the financing from TESCAN CHINA, Ltd.

## Data Availability

The diffraction patterns of the unstrained polycrystal Al-Mg alloy of tilt angles  $60^\circ$  and  $65^\circ$  are available at Zenodo (DOI: 10.5281/zenodo.7528088), and the patterns of sample tilt  $70^\circ$  are also shared at Zenodo (DOI: 10.5281/zenodo.6990325). The indexation results for all these data are also provided, including the crystal orientations and calibrated PC coordinates, with the full pattern or its gradients. We invite interested colleagues to use this dataset to further improve the calibration of EBSD. The other data will be made available on request.

## References

- [1] S.I. Wright and B.L. Adams. Automatic analysis of electron backscatter diffraction patterns. *Metallurgical Transactions A*, 23(3):759–767, 1992.
- [2] D. Jha, S. Singh, R. Al-Bahrani, W. Liao, A. Choudhary, M. De Graef, and A. Agrawal. Extracting grain orientations from EBSD patterns of polycrystalline materials using convolutional neural networks. *Microscopy and Microanalysis*, 24(5):497–502, 2018.
- [3] Y.H. Chen, S.U. Park, D. Wei, G. Newstadt, M.A. Jackson, J.P. Simmons, M. De Graef, and A.O. Hero. A dictionary approach to electron backscatter diffraction indexing. *Microscopy and Microanalysis*, 21(3):739–752, 2015.
- [4] A.J. Wilkinson, G. Meaden, and D.J. Dingley. High-resolution elastic strain measurement from electron backscatter diffraction patterns: New levels of sensitivity. *Ultramicroscopy*, 106(4-5):307 – 313, 2006.
- [5] A. J. Wilkinson and T. B. Britton. Strains, planes, and EBSD in materials science. *Materials Today*, 15:366–376, 2012.

- [6] E. Plancher, J. Petit, C. Maurice, V. Favier, L. Saintoyant, D. Loinsard, N. Rupin, J.-B. Marijon, O. Ulrich, M. Bornert, J.-S. Micha, O. Robach, and O. Castelnau. On the accuracy of elastic strain field measurements by Laue microdiffraction and high-resolution EBSD: a cross-validation experiment. *Experimental Mechanics*, 56(3):483–492, 2016.
- [7] T. Vermeij and J.P.M. Hoefnagels. A consistent full-field integrated DIC framework for HR-EBSD. *Ultramicroscopy*, 191:44 – 50, 2018.
- [8] T.J. Ruggles, G.F. Bomarito, R.L. Qiu, and J.D. Hochhalter. New levels of high angular resolution EBSD performance via inverse compositional Gauss-Newton based digital image correlation. *Ultramicroscopy*, 195:85 – 92, 2018.
- [9] Q. Shi, S. Roux, F. Latourte, and F. Hild. Estimation of elastic strain by integrated image correlation on electron diffraction patterns. *Ultramicroscopy*, 199:16–33, 2019.
- [10] C. Ernould, B. Beausir, J.-J. Fundenberger, V. Taupin, and E. Bouzy. Global DIC approach guided by a cross-correlation based initial guess for HR-EBSD and on-axis HR-TKD. *Acta Materialia*, 191:131 – 148, 2020.
- [11] C. Maurice, R. Fortunier, J. Driver, A. Day, K. Mingard, and G. Meaden. Comments on the paper "Bragg's law diffraction simulations for electron backscatter diffraction analysis" by Josh Kacher, Colin Landon, Brent L. Adams and David Fullwood. 110(7):758 – 759.
- [12] D. Dingley and K. Baba-Kishi. Use of electron back scatter diffraction patterns for determination of crystal symmetry elements. *Scanning Electron Microscopy*, 1986(2), 1986.
- [13] J. Venables and R. Bin-jaya. Accurate microcrystallography using electron back-scattering patterns. *Philosophical Magazine*, 35(5):1317–1332, 1977.
- [14] D.A. Carpenter, J.L. Pugh, G.D. Richardson, and L.R. Mooney. Determination of pattern centre in EBSD using the moving-screen technique. *Journal of Microscopy*, 227(3):246–247, 2007.
- [15] T.B. Britton, C. Maurice, R. Fortunier, J.H. Driver, A.P. Day, G. Meaden, D.J. Dingley, K. Mingard, and A.J. Wilkinson. Factors affecting the accuracy of high resolution electron backscatter diffraction when using simulated patterns. *Ultramicroscopy*, 110(12):1443 – 1453, 2010.
- [16] C. Maurice, K. Dzieciol, and R. Fortunier. A method for accurate localisation of EBSD pattern centres. *Ultramicroscopy*, 111(2):140 – 148, 2011.
- [17] BLG PRODUCTIONS LTD. Methods, apparatuses and computer programs for crystallography, 10 2012.
- [18] K. Lassen and J. Bilde-Sørensen. Calibration of an electron back-scattering pattern set-up. *Journal of Microscopy*, 170(2):125–129.
- [19] Y. Zhang, S. Fang, C. Lin, J. Zhang, C. Jiang, Y. Zeng, F. Huang, and H. Miao. A new method for locating Kikuchi bands in electron backscatter diffraction patterns. *Microscopy Research and Technique*, 82(12):2035–2041, 2019.

- [20] Y. Zhang, Y. Shen, F. Peng, C. Jiang, W. Li, H. Miao, F. Huang, and Y. Zeng. Method for acquiring accurate coordinates of the source point in electron backscatter diffraction. *Journal of Microscopy*, 284(3):233–243, 2021.
- [21] B.E. Jackson, J.J. Christensen, S. Singh, M. De Graef, D.T. Fullwood, E.R. Homer, and R.H. Wagoner. Performance of dynamically simulated reference patterns for cross-correlation electron backscatter diffraction. *Microscopy and Microanalysis*, 22(4):789–802, 2016.
- [22] J. Basinger, D. Fullwood, J. Kacher, and A. Brent. Pattern center determination in electron backscatter diffraction microscopy. *Microscopy and Microanalysis*, 17(3):330–340, 2011.
- [23] S. Vespucci, G. Naresh-Kumar, C. Trager-Cowan, K. P. Mingard, D. Maneuski, V. O’Shea, and A. Winkelmann. Diffractive triangulation of radiative point sources. *Applied Physics Letters*, 110(12):124103, 2017.
- [24] G. Nolze, M. Jürgens, J. Olbricht, and A. Winkelmann. Improving the precision of orientation measurements from technical materials via EBSD pattern matching. *Acta Materialia*, 159:408 – 415, 2018.
- [25] E.L. Pang, P.M. Larsen, and C.A. Schuh. Global optimization for accurate determination of EBSD pattern centers. *Ultramicroscopy*, 209:112876, 2020.
- [26] A. Foden, D.M. Collins, A.J. Wilkinson, and T.B. Britton. Indexing electron backscatter diffraction patterns with a refined template matching approach. *Ultramicroscopy*, 207:112845, 2019.
- [27] T. Tanaka and A.J. Wilkinson. Pattern matching analysis of electron backscatter diffraction patterns for pattern centre, crystal orientation and absolute elastic strain determination - accuracy and precision assessment. *Ultramicroscopy*, 202:87–99, 2019.
- [28] Q. Shi, D. Loisonard, C. Dan, F. Zhang, H. Zhong, H. Li, Y. Li, Z. Chen, H. Wang, and S. Roux. Calibration of crystal orientation and pattern center of EBSD using integrated digital image correlation. *Materials Characterization*, 178:111206, 2021.
- [29] T. Friedrich, A. Bochmann, J. Dinger, and S. Teichert. Application of the pattern matching approach for EBSD calibration and orientation mapping, utilising dynamical EBSP simulations. *Ultramicroscopy*, 184:44 – 51, 2018.
- [30] P. Callahan and M. Graef. Dynamical electron backscatter diffraction patterns. part i: Pattern simulations. *Microscopy and microanalysis*, 19:1–11, 2013.
- [31] A. Winkelmann and G. Nolze. Analysis of kikuchi band contrast reversal in electron backscatter diffraction patterns of silicon. *Ultramicroscopy*, 110:190–194, 2010.
- [32] Q. Shi, E. Plancher, D. Loisonard, P. Karamched, J. Liu, Z. Chen, H. Wang, and S. Roux. Improved high-resolution EBSD analyses by correcting radial distortion of electron diffraction patterns. *Materials Characterization*, 194:112458, 2022.

- [33] F. Ram and M. Graef. Energy dependence of the spatial distribution of inelastically scattered electrons in backscatter electron diffraction. *Physical review. B, Condensed matter*, 97:134104, 2018.
- [34] A. Winkelmann. Dynamical effects of anisotropic inelastic scattering in electron backscatter diffraction. *Ultramicroscopy*, 108(12):1546–1550, 2008.
- [35] A. Winkelmann, G. Nolze, G. Cios, T. Tokarski, P. Bala, B. Hourahine, and C. Trager-Cowan. Kikuchi pattern simulations of backscattered and transmitted electrons. *Journal of Microscopy*, 284(2):157–184, 2021.
- [36] J. Alkorta, M. Marteleur, and P.J. Jacques. Improved simulation based HR-EBSD procedure using image gradient based DIC techniques. *Ultramicroscopy*, 182:17 – 27, 2017.
- [37] N. Saowadee, K. Agersted, and J. Bowen. Lattice constant measurement from electron backscatter diffraction patterns. *Journal of Microscopy*, 266(2):200–210, 2017.
- [38] G. Nolze, T. Tokarski, L. Rychłowski, G. Cios, and A. Winkelmann. Crystallographic analysis of the lattice metric (CALM) from single electron backscatter diffraction or transmission Kikuchi diffraction patterns. *Journal of Applied Crystallography*, 54(3):1012–1022, 2021.
- [39] F. Hild and S. Roux. Digital image correlation. In P. Rastogi and E. Hack, editors, *Optical Methods for Solid Mechanics. A Full-Field Approach*, pages 183–228. Wiley-VCH, Weinheim (Germany), 2012.
- [40] Q. Shi, Y. Zhou, H. Zhong, D. Loizard, C. Dan, F. Zhang, Z. Chen, H. Wang, and S. Roux. Indexation of electron diffraction patterns at grain boundaries. *Materials Characterization*, 182:111553, 2021.
- [41] C. Maurice and R. Fortunier. A 3D Hough transform for indexing EBSD and Kossel patterns. *Journal of Microscopy*, 230(3):520–529, 2008.
- [42] F. Ram, S. Zaefferer, and D. Raabe. Kikuchi bandlet method for the accurate deconvolution and localization of Kikuchi bands in Kikuchi diffraction patterns. *Journal of Applied Crystallography*, 47(1):264–275, 2014.
- [43] M. Mollens, S. Roux, F. Hild, and A. Guery. Insights into a dual-phase steel microstructure using EBSD and image-processing-based workflow. *Journal of Applied Crystallography*, 55(3):601–610, 2022-06.
- [44] K. Mingard, A. Day, C. Maurice, and P. Queded. Towards high accuracy calibration of electron backscatter diffraction systems. *Ultramicroscopy*, 111(5):320 – 329, 2011.
- [45] H. Zhong, Q. Shi, Z. Chen, C. Dan, S. Zhong, and H. Wang. Residual-based pattern center calibration in high-resolution electron backscatter diffraction. *Micron*, 146:103081, 2021.
- [46] A. Winkelmann, G. Nolze, G. Cios, T. Tokarski, and P. Bała. Refined calibration model for improving the orientation precision of electron backscatter diffraction maps. *Materials*, 13:2816, 2020.
- [47] Q. Shi, L. Jiao, D. Loizard, C. Dan, Z. Chen, H. Wang, and S. Roux. Improved EBSD indexation accuracy by considering energy distribution of diffraction patterns. *Materials Characterization*, 188:111909, 2022.